Electronic Supplementary Material (ESI) for Energy & Environmental Science.
This journal is © The Royal Society of Chemistry 2017

Supporting Materials

For *Energy & Environmental Science*

Structural origin of enhanced piezoelectric performance and stability in lead free ceramics

Ting Zheng[1,#], Haijun Wu[2, #], Yuan Yuan[1, #], Xiang Lv[1], Qi Li[3], Tianlu Men[3], Chunlin Zhao[1], Dingquan Xiao[1], Jiagang Wu[1,*], Ke Wang[3,*], Jingfeng Li[3], Yueliang Gu[4], Jianguo Zhu[1], and Stephen J. Pennycook[2,*]

[1]*Department of Materials Science, Sichuan University, 610064, Chengdu, P. R. China*

[2]*Department* of Materials Science and Engineering, National University of Singapore, 117575, Singapore

[3]*State Key Laboratory of New Ceramics and Fine Processing, School of Materials Science and Engineering, Tsinghua University, 100084, Beijing, P. R. China*

[4]*Shanghai Synchrotron Radiation Facility, Shanghai Institute of Applied Physics, Chinese Academy of Sciences, Pudong New Area, Shanghai 201204, P. R. China*

# Equal contribution

* Corresponding author:

wujiagang0208@163.comand mswujg@scu.edu.cn (Jiagang Wu)

steve.pennycook@nus.edu.sg (Stephen J. Pennycook) wang-ke@tsinghua.edu.cn (Ke Wang)

1. Experiment equipment

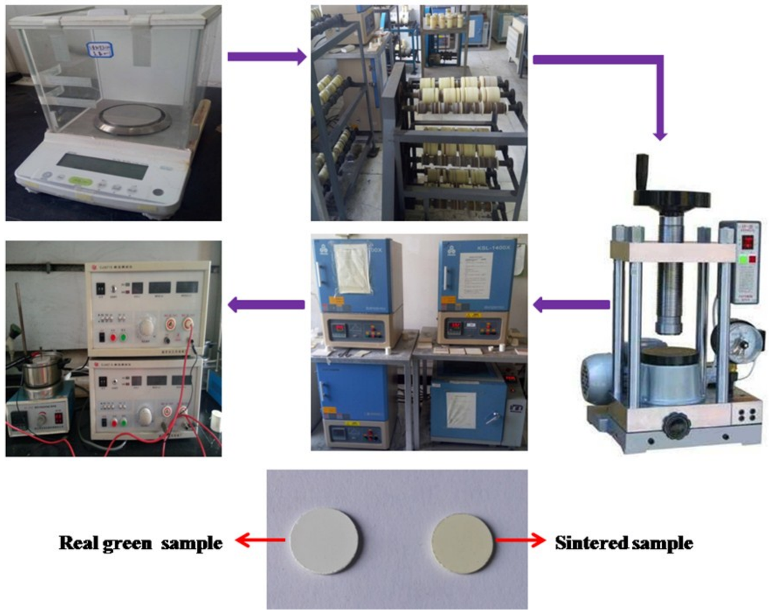

Figure S1: Images of overall processing equipment and pictures of real green and sintered samples fabricated in this study.

2. Phase structure

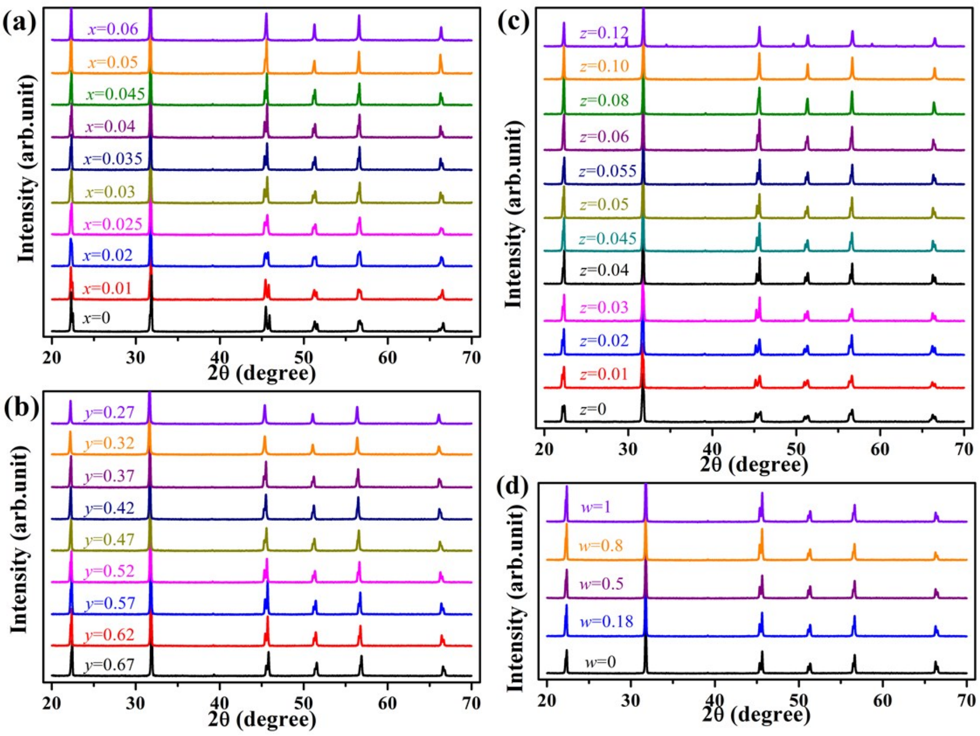

Figure S2: XRD patterns of the ceramics with different (a) *x*, (b) *y*, (c) *z*, and (d) *w*.

Figure S2 shows the XRD patterns of the ceramics as a function of (a) x, (b) y, (c) z, and (d) w content, measured at 20 °C and 2θ=20~70°. It can be seen that all the samples have a pure perovskite structure without impurity phases except for z=0.12 due to excessive Sb content.

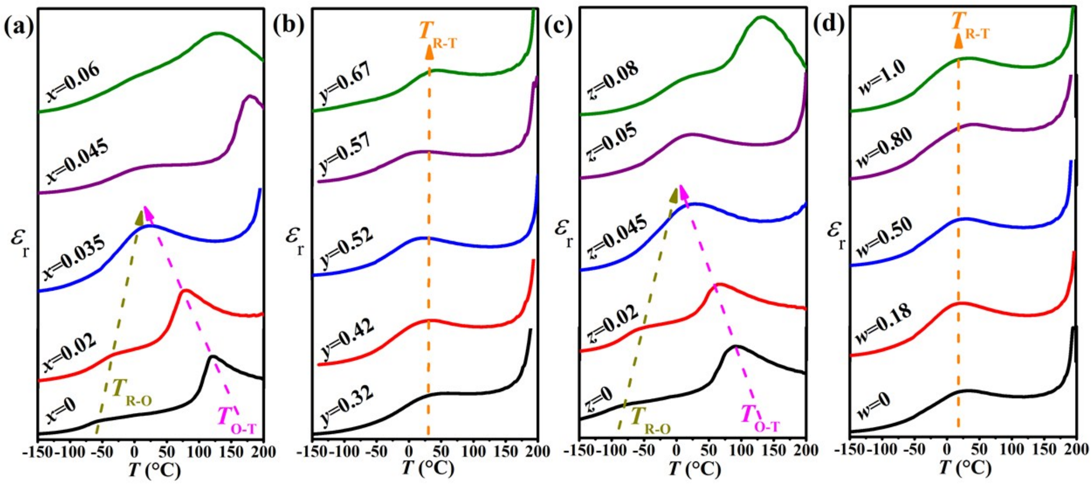

Figure S3: temperature -dependent dielectric curves of the $(1-x)(K_{1-y}Na_y)(Nb_{1-z}Sb_z)O_3$ $-xBi_{0.5}(Na_{1-w}K_w)_{0.5}HfO_3$ ceramics as a function of (a) x, (b) y, (c) z, and (d) w, measured at -150 to 200 °C and f=100 kHz.

Figure S3 shows the ε_r-T curves of the $(1-x)(K_{1-y}Na_y)(Nb_{1-z}Sb_z)O_3$ $-xBi_{0.5}(Na_{1-w}K_w)_{0.5}HfO_3$ ceramics as a function of (a) x, (b) y, (c) z, and (d) w, measured from -150 °C to 200 °C and f=100 kHz. As shown in Figs. S3 (a) and (c), the addition of BNKH (x) and Sb (z) will increase T_{R-O} and decrease T_{O-T} simultaneously, and then leading to the formation of R-T phase boundary at room temperature. However, the phase transition temperature (T_{R-T}) almost has no changes with the variation of K/Na ratio, as shown in Figs. S3(b) and (d).

3. Electrical properties

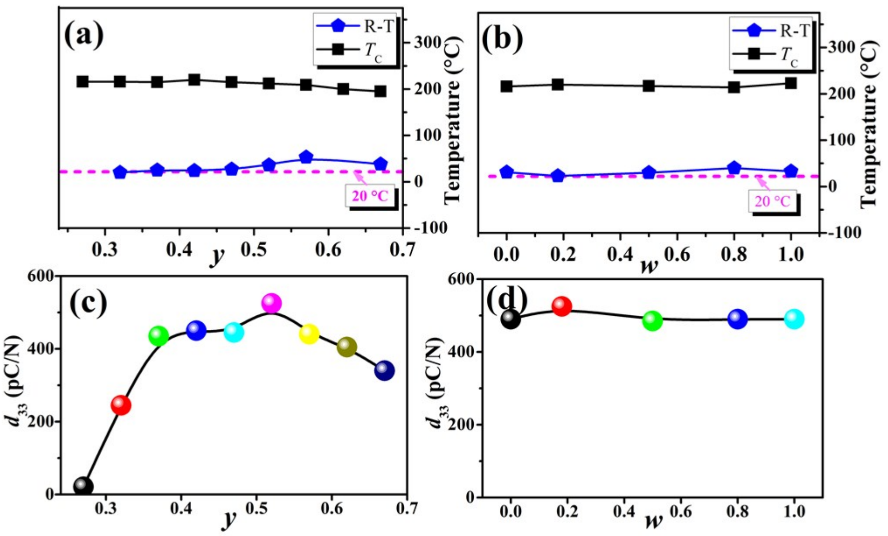

Figure S4: (a,b) phase diagram (c,d) d_{33} of the $0.965(K_{1-y}Na_y)(Nb_{0.95}Sb_{0.05})O_3$ - $0.035Bi_{0.5}(Na_{1-w}K_w)_{0.5}HfO_3$ ceramics as a function of y and w

Figures S4(a) and (b) show the phase diagrams of the $0.965(K_{1-y}Na_y)(Nb_{0.95}Sb_{0.05})O_3$ - $0.035Bi_{0.5}(Na_{1-w}K_w)_{0.5}HfO_3$ ceramics as a function of y (x=0.035, z=0.05, w=0.18) and w (x=0.035, y=0.48, z=0.05), respectively. It can be observed that the variation of K/Na ratio in KNN –based ceramics has no big influence on the phase transition temperature (T_C and T_{R-T}). Correspondingly, their piezoelectricity can maintain a high value in the R-T phase boundary region, as shown in Figs. S4(c) and (d).

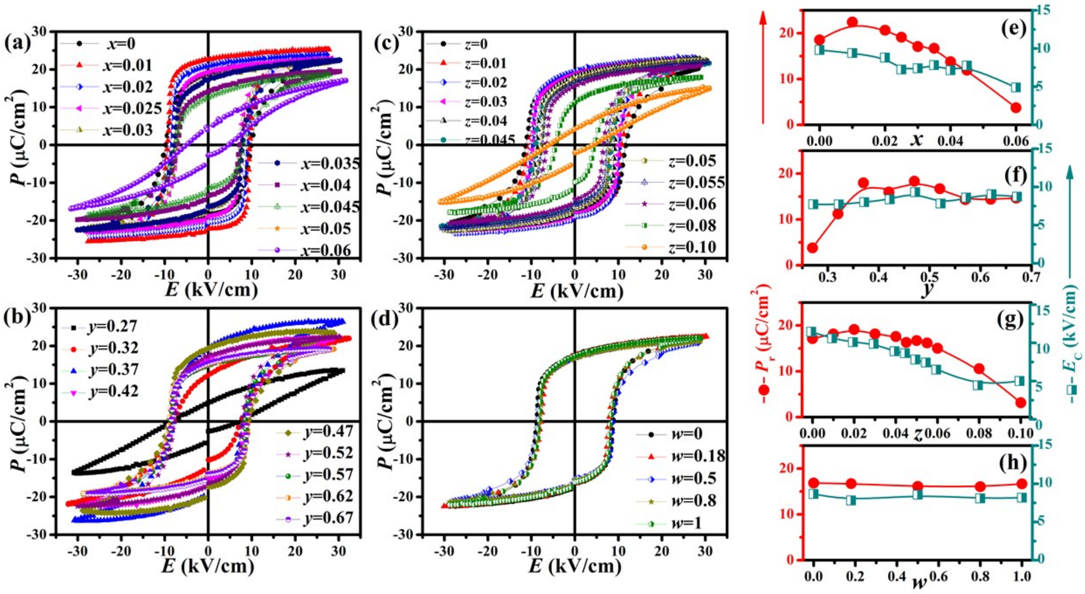

Figure S5: *P*-*E* loops and corresponding P_r and E_C values of the ceramics as a function of (a, e) *x*, (b, f) *y*, (c, g) *z*, and (d, h) *w* content.

Figure S5 shows the ferroelectric properties of $(1\text{-}x)(K_{1\text{-}y}Na_y)(Nb_{1\text{-}z}Sb_z)O_3$ -$x$$Bi_{0.5}(Na_{1\text{-}w}K_w)_{0.5}HfO_3$ ceramics as a function of *x*, *y*, *z*, and *w* contents, measured at 20 ^oC and *f*=10 Hz. It can be obviously observed from Figs. S5(a~d) that typical *P*-*E* hysteresis loops can be attained and their curve shapes are closely related to the compositions. In order to investigate the composition dependence of ferroelectric properties, their P_r and E_C values derived from the corresponding *P*-*E* loops were shown here. As shown in Figs S5 (e) and (g), their P_r and E_C values decrease gradually with the increase of *x* and *z* contents. In addition, the P_r and E_C values of the ceramics with different K/Na ratio fluctuate within a certain range and remain unchanged, respectively, as shown in Figs S5 (f) and (h).

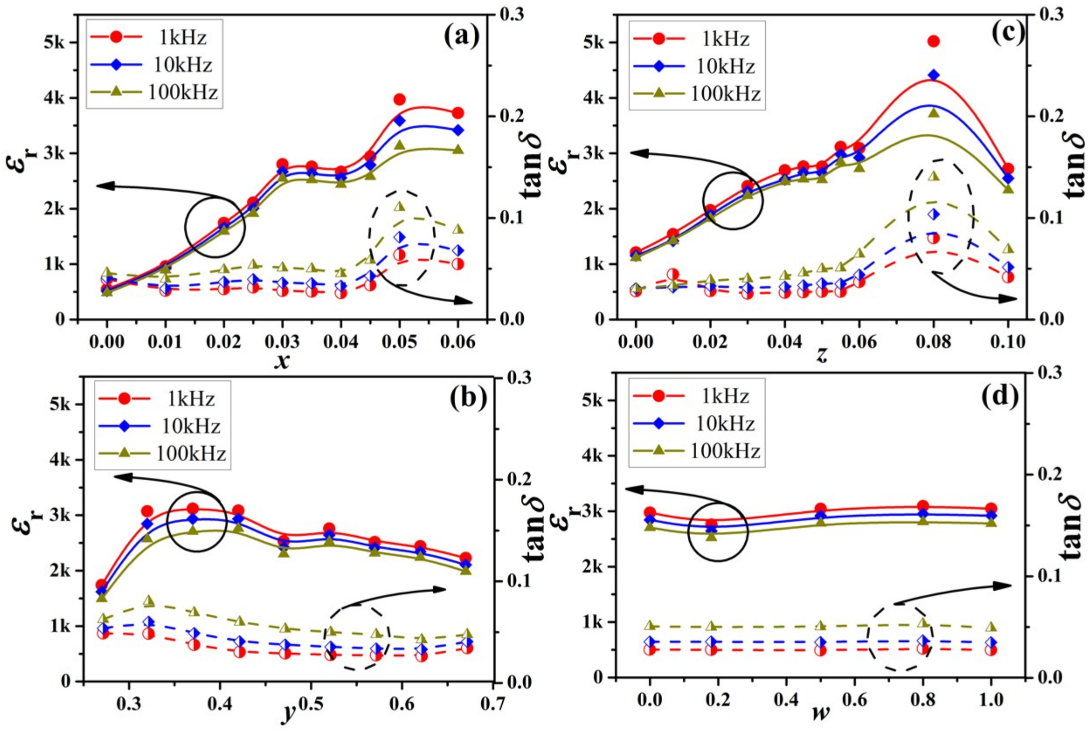

Figure S6: dielectric properties of the ceramics as a function of (a) *x*, (b) *y*, (c) *z*, and (d) *w* content.

Figure S6 shows the dielectric properties of the ceramics with different *x*, *y*, *z*, and *w* contents, measured at 20 ^{o}C and *f*=1, 10, and 100 kHz. Consistence with the variations of ferroelectricity, the composition also determines their dielectric properties. As shown in Fig. S6(a~c), ε_r gradually increases as the increase of *x*, *y*, and*z* contents. However, there is almost no change for the ceramics with different *w* contents, as shown in Fig. S6(d). In addition, the tan δ of the ceramics with different *x* and *z* contents can be maintained at a relatively stable value in the low-doping content, and then increases sharply for the ceramics with high *x* and *z* contents. However, it seems that the tan δ is independent on the K/Na ratio in this material system.

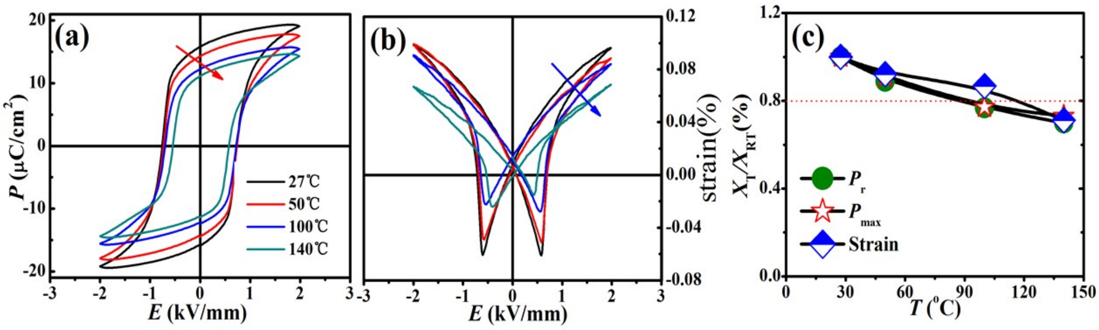

Figure S7: (a) Polarization hysteresis $P(E)$ loops and (b) bipolar strain $S(E)$ curves of the ceramics with x=0.035, y=0.52, z=0.05 and w=0.18, measured at different temperatures. (c) Temperature dependence of P_{max}, P_r, and strain of the ceramics with x=0.035, y=0.52, z=0.05 and w=0.18.

Figures S7 (a) and (b) show the polarization hysteresis $P(E)$ loops and bipolar strain $S(E)$ curves of the ceramics, measured at 2 kV/mm and different temperatures. Typical and saturated P-E and S-E loops can be observed in the ceramics under various measurement temperatures. As shown in Fig. S7(a), the maximum and remanent polarization (P_{max} and P_r) values reduce gradually with the increase of measurement temperatures. While their coercive field (E_C) values almost have no changes when the measurement temperatures increase from 27 °C to 100 °C, and then have a decrease until 140 °C. Previously, it was reported that a high processing temperature will help to reduce the E_C values due to the easier domain switching and polarization reversal caused by thermally activated process. However, E_C will increase when temperature is enhanced away from PPT. Therefore, the enlargement of E_C due to the deviation from R-T phase boundary region will neutralize the reduction of E_C induced by thermally activated process, resulting in the unchanged E_C value in the temperature range of 27 ~100 °C. As shown in Fig. S7(b), the bipolar strain properties have a similar changing trend with respect to the temperature dependence of ferroelectricity.Figure S7(c) summaries the temperature stability of P_r, P_{max}, and bipolar strain values, which derived from the temperature dependence of polarization hysteresis $P(E)$loops and bipolar strain $S(E)$ curves. Good temperature stability of P_r, P_{max}, and bipolar strain can be attained. The X_T/X_{RT} values can still maintain 70% even if the temperature reaches 140 ^oC. Thus an improved temperature stability of ferroelectricity has been obtained in the ceramics.

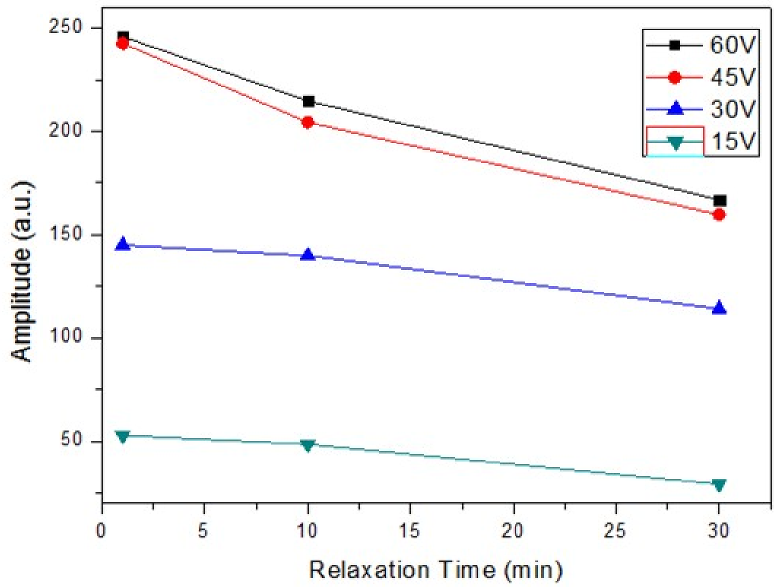

Figure S8: Amplitude *vs* relaxation time of the ceramics with x=0.035, y=0.52, z=0.05 and w=0.18 as a function of voltage.

As shown in Fig. S8, the higher the voltage, the better the polarization. When the applied voltage is greater than 45 V, nearly saturated polarization can be obtained. Besides, amplitude decreases gradually with the increase of relaxation time, indicating that the relaxation characteristics have been occurred.

4. TEM results

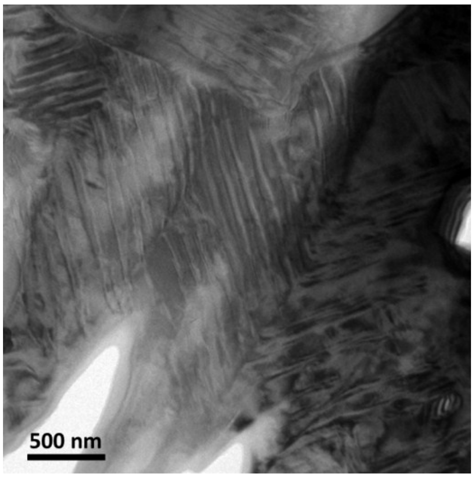

Figure S9. TEM image shows several groups of sub-micro domains with different orientations.

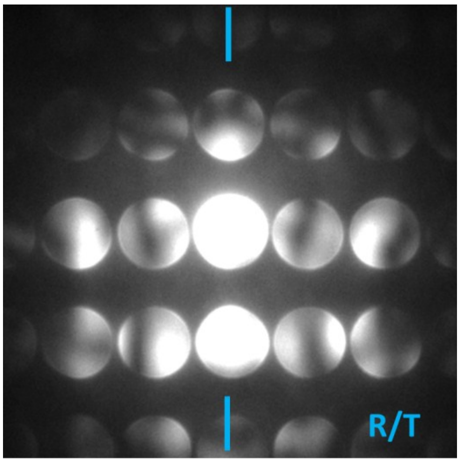

Figure S10. CBED pattern along [110] zone axis shows mirror plane along [1-10], reflecting R or T symmetry.

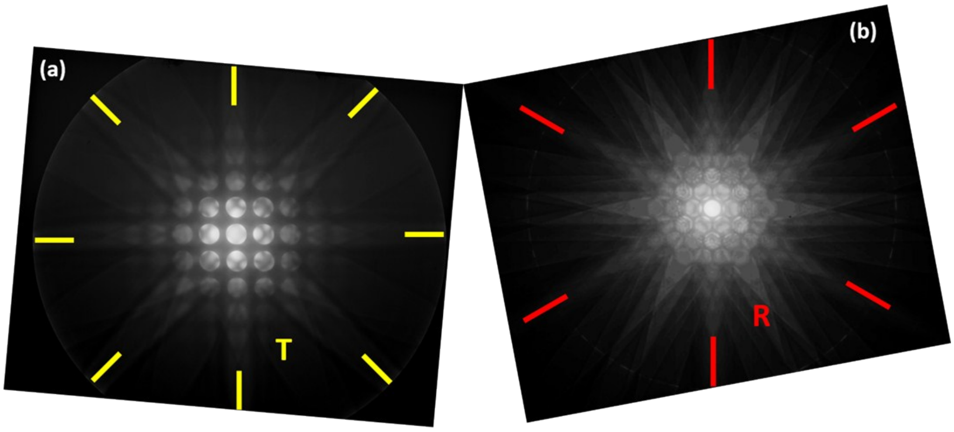

Figure S11: Whole CBED patterns along [001] and [111] zone axis showing 4mm and 3m symmetry, respectively. Figure 6(e) and 6(f) are cut from them.

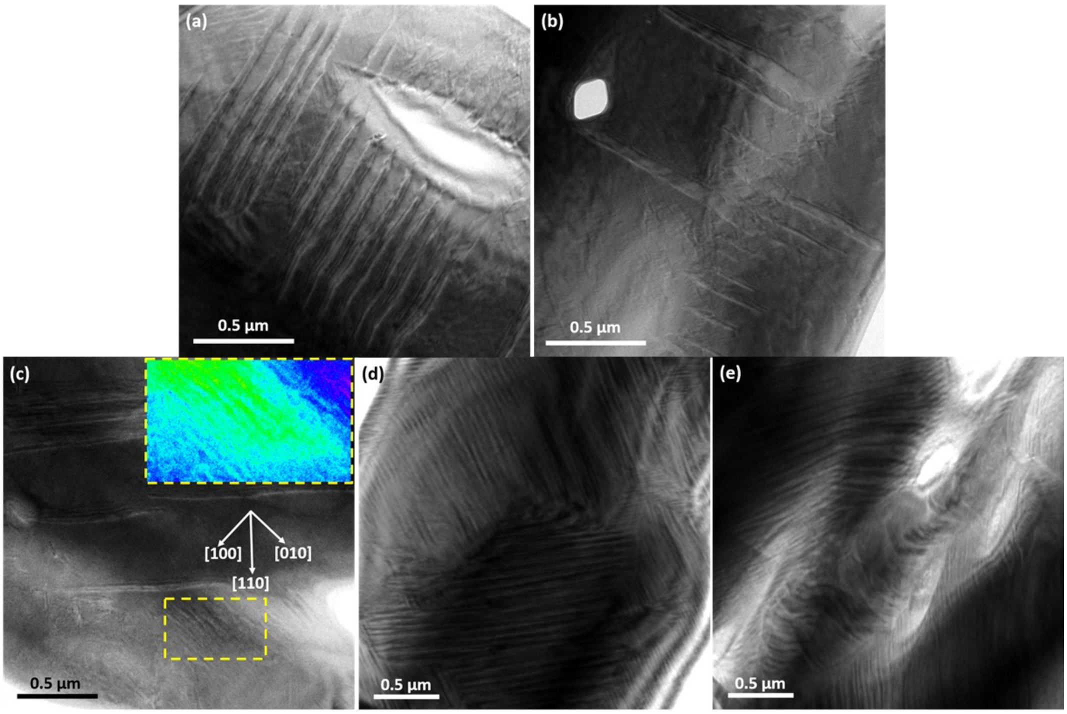

Figure S12: TEM images showing nanodoamains: (a-b) obtained close to the two-beam condition; (c-e) obtained along normal orientation.

The hierarchical domain pattern can only be seen along particular orientation (e.g., two-beam condition) in TEM. For two-beam conditions, the reciprocal lattice is rotated by appropriate double tilt (X and Y) so that a particular g(hkl) satisfying the Weiss zone law is brought exactly on the Ewald sphere. This makes that particular diffraction spot (e.g., corresponding to the nanodomains in the present case) as intense as the central beam. The hierarchical domain pattern in Figure 6awas just acquired under this condition, and we also provides other images taken from different areas of different samples in Figure S12 (a,b). However, if observing from normal orientations away from the two-beam condition, the hierarchicalnanodomains will turn to nanodomains with one or two orientations but without sub-micro domain boundary (i.e., without hierarchical feature), as shown in Figure S12 (c-e).

Table S1. The detailed symmetry elements of tetragonal (T), Orthorhombic (O) and rhombohedral (R) phases. The symbol “4” and “3” mean 4-fold and 3-fold rotation; “m” means a mirror plane; “c” means a glide.

Phase	space group	Lattice type	Point group	Ps	Symmetry Direction		
					Primary	Secondary	Tertiary
Tetragonal (T)	P4mm	primitive (P)	4mm	[001]	“4” along [001]	“m” along [100]/[010]	“m” along [110]/[1-10]
Orthorhombic (O)	Amm2	Single-face centered (A)	mm2	[110]	“m” along [100]	“m” along [010]	“m” along [001]
Rhombohedral (R)	R3c	rhombohedrally centered	3m	[111]	“3” along [111]	“c” along [111]	-

Table S2. CBED symmetry existing along [001], [110] and [111] pseudocubic zone axes for tetragonal (T) and rhombohedral (R) with different polarization directions. The symbol “m” stands for a mirror plane, “1_R” stands for a mirror plane perpendicular to the incidence, and “No” indicates no symmetry.

Phase	Polarization direction	Pseudocubic zone axis					
		[001]		[110]		[111]	
T **(P4mm)**	[100]	mI_R m//[100]	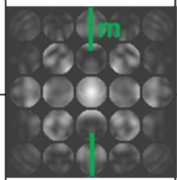	m m//[1-10]	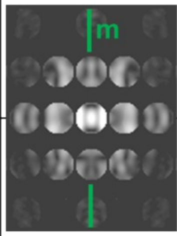	m m//[-211]	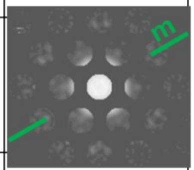
	[010]	mI_R m//[010]		m m//[1-10]		m m//[1-21]	
	[001]	4mm m//[100] m//[010] m//[110] m//[1-10]	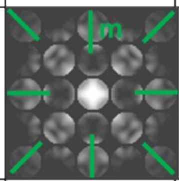	mI_R m//[001]	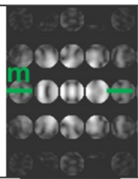	m m//[11-2]	
R **(R3m)**	[111] and [11-1]	m m//[110]	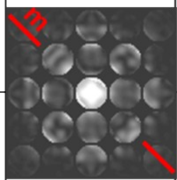	m m//[001]	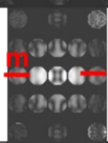	3m m//[11-2] m//[1-21] m//[-211]	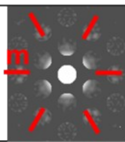
	[-111] and [1-11]	m m//[1-10]		I_R	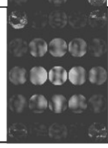	m m//[-211]